AGU PUBLICATIONS

Geophysical Research Letters

RESEARCH LETTER
10.1002/2015GL067566

Key Points:
- Swells are systematically tracked using synthetic aperture radar from the Envisat mission
- A robust range of the swell dissipation is calculated and can be used to constrain air-sea fluxes
- Swell dissipation is weakly related to its steepness and wind speed weighted by the direction

Supporting Information:
- Supporting Information S1

Correspondence to:
J. E. Stopa,
justin.stopa@ifremer.fr

Citation:
Stopa, J. E., F. Ardhuin, R. Husson, H. Jiang, B. Chapron, and F. Collard (2016), Swell dissipation from 10 years of Envisat advanced synthetic aperture radar in wave mode, *Geophys. Res. Lett.*, *43*, 3423–3430, doi:10.1002/2015GL067566.

Received 24 DEC 2015
Accepted 21 MAR 2016
Accepted article online 24 MAR 2016
Published online 9 APR 2016

Swell dissipation from 10 years of Envisat advanced synthetic aperture radar in wave mode

Justin E. Stopa[1], Fabrice Ardhuin[1], Romain Husson[2], Haoyu Jiang[3], Bertrand Chapron[1], and Fabrice Collard[4]

[1]University Brest, CNRS, IRD, Ifremer, Laboratoire d'Oceanographie Physique et Spatiale (LOPS), IUEM, Brest, France, [2]Collecte Localisation Satellites, Plouzane, France, [3]College of Information Science and Engineering, Ocean University of China, Qingdao, China, [4]Ocean Data Lab, Plouzane, France

Abstract Swells are found in all oceans and strongly influence the wave climate and air-sea processes. The poorly known swell dissipation is the largest source of error in wave forecasts and hindcasts. We use synthetic aperture radar data to identify swell sources and trajectories, allowing a statistically significant estimation of swell dissipation. We mined the entire Envisat mission 2003–2012 to find suitable storms with swells ($13 < T < 18$ s) that are observed several times along their propagation. This database of swell events provides a comprehensive view of swell extending previous efforts. The analysis reveals that swell dissipation weakly correlates with the wave steepness, wind speed, orbital wave velocity, and the relative direction of wind and waves. Although several negative dissipation rates are found, there are uncertainties in the synthetic aperture radar-derived swell heights and dissipation rates. An acceptable range of the swell dissipation rate is -0.1 to 6×10^{-7} m^{-1} with a median of 1×10^{-7} m^{-1}.

1. Introduction

Wind waves created by severe storms propagate away from their generation area as swells, which are an important component of the wave climate prevalent in all basins of the global ocean [e.g., *Snodgrass et al*., 1966; *Chen et al*., 2002; *Alves*, 2006]. These long waves can travel large distances with little loss of energy [*Barber and Ursell*, 1948; *Munk*, 1947; *Munk et al*., 1963]. Swells have direct effects on the Earth system and human activities even in the far-field of storms. Swells influence seagoing activities like ship routing and port operations. Due to their long periods, swells can produce significant runup which causes erosion and coastal damage [e.g., *Lefevre*, 2009; *Hoeke et al*., 2013]. Swells also contribute to the energy and momentum fluxes at the air-sea boundary [e.g., *Fairall et al*., 2003; *Semedo et al*., 2009]. Far from the generation region, swells radiate energy that travels at the group speed of linear waves, along great circle routes [*Barber and Ursell*, 1948]. The dispersion of wave energy in space and time is the main reason of the attenuation of swell heights, without any dissipation of energy. These effects from both frequency dispersion and angular spreading are modeled by propagating waves on an idealized sphere [*Collard et al*., 2009]. Still, a detailed energy balance reveals that swells also dissipate, and wave energy is lost to the environment, via mechanisms that are still unclear. *Snodgrass et al*. [1966] suggested that wind, wind wave breaking, or nonlinear interactions might be important, while *Ardhuin et al*. [2009] attributed the dissipation to friction at the air-sea interface. Alternatively, *Babanin* [2006] suggested that the energy lost by the swells could be a source of mixing in the upper ocean, but this has yet to be quantified.

How can we test these ideas? A discrimination of dissipation mechanisms is very difficult in the laboratory because the dissipation rates are so weak that they cannot be measured [e.g., *Harris*, 1966; *Young and Sobey*, 1985; *Babanin and Haus*, 2009]. Also, the range of parameters may be outside of what is possible in the laboratory. In particular, the transition of the atmospheric boundary layer from the laminar to turbulent regimes may happen for wave heights exceeding 2 m. Alternatively, numerical simulations may provide useful guidance on probable mechanisms, but important factors such as the dynamic roughness and pressure effects from the wind must be incorporated before realistic rates are determined [e.g., *Perignon et al*., 2014]. Finally, field experiments are very few and based on limited samples. *Snodgrass et al*. [1966] estimated swell decay using in situ observations, but their array was limited to near-shore locations that are affected by swell dissipation at shorelines. In the measurements of *Högström et al*. [2009], the upward momentum flux can be related to a swell dissipation rate. Here we use synthetic aperture radar (SAR) to track and estimate the spatial decay rate of swells. Since ERS-1, and today with Sentinel-1 [e.g., *Ardhuin et al*., 2015], European

Space Agency SARs have operated in a "wave mode" for a global mapping of swell fields [*Hasselmann et al*., 2012]. It was initially demonstrated by *Holt et al*. [1998], *Heimbach and Hasselmann* [2000], and *Lehner et al*. [2000] that swells can be tracked using SAR. *Collard et al*. [2009] enhanced their approach and exploited the high space-time coherence of swells to quantitatively estimate swell dissipation. The analysis of dissipation rates was performed by *Ardhuin et al*. [2009] but was limited to 22 events. Here our goal is to analyze the variability of swell dissipation rates by using the full history of Envisat's SAR data from January 2003 to April 2012 and analyze more than 1000 events.

Dissipation rates are calculated from swell heights, wavelengths, and directions derived from Envisat, following the method of *Collard et al*. [2009]. We describe our data set, swell tracking procedure, and method of calculating the swell dissipation rate in section 2. Next we present the swell dissipation rates in section 3, and our discussion and conclusion follow in section 4.

2. Swell Tracking and Dissipation

2.1. Swell Tracking

We use wave spectra (level 2) derived from Envisat advanced synthetic aperture radar (ASAR) wave mode. The satellite footprint is 10×7 km with a nominal spatial resolution of 9×6 m and samples every 200 km along track in a 35 day repeat orbit. The high-frequency random surface motions reduce the SAR's nominal azimuthal resolution and leads to a blurring effect [*Kerbaol et al*., 1998; *Stopa et al*., 2015a]. This is called the azimuth cutoff and is strongly correlated with the wind seas. Therefore, the wind speed and the azimuth cutoff help remove the wind sea component before the quasi-linear inversion maps the images to wave spectra [*Chapron et al*., 2001]. The spectra are partitioned using a watershed method similar to *Portilla et al*. [2009] to provide the swell components of significant wave height (H_{ss}), wave period (T), and direction (θ_p). These are the essential parameters used to track swells, and they compare well with buoys having root-mean-square errors less than 0.4 m, 20°, and 50 m for H_{ss}, θ_p, and wavelength, respectively [*Collard et al*., 2009].

We restrict the SAR observations to the best quality data. When the wind speed and azimuth cutoff are large, the spectral components can be directionally distorted and the H_{ss} can be inaccurate. Therefore, we only use SAR data when the wind speed is between 3 and 9 m/s and when the swell wavelength exceeds the azimuth cutoff, to ensure the swell is properly resolved. We also exclude images with normalized variances larger than 1.5, which eliminates contamination from anomalous objects like ships, islands, or slicks.

We track swells using the two-step approach of *Collard et al*. [2009] and *Husson* [2012]. First, we identify the swell generation source, and second, we track wave packets of a given frequency and direction. Sources are identified by propagating the waves backward at their group velocities (Cg) along great circles until they converge in space and time. This convergence is defined by the density map of intersecting back-propagated waves in time and space. The maximum density defines the swell source location and time. The duration and approximate storm size is estimated from these density maps. The storm radius is defined as the average distance from the density maximum outward to regions with a minimum of five swell partitions [*Husson*, 2012]. Storms with smaller diameters best approximate a point source for which the dispersion model is well defined. Therefore, we limit our data set to storms with diameters less than 1500 km and with durations less than 24 h.

The second step tracks wave packets forward in time from their source by propagating a given group velocity and direction along a great circle route. SAR data are retained when the wavelength and direction are within 50 m and 20° of the assumed wave trajectory. This procedure is repeated for all possible wave directions and periods. Due to frequency dispersion, the longest waves propagate in front of the swell train. We remove swell partitions that do not follow this rule and that usually correspond to multiple sources. The last step groups the SAR observations into tracks with wavelength and directional bands less than 40 m and 10°. We require each track contains at least 15 observations from 5 different satellite passes and span distances of 3000 km. These constraints ensure a statistically reliable decay rate. The grouped SAR observations represent the evolution of a wave packet from the generation source, and these data are required to accurately estimate dissipation.

2.2. Swell Dissipation

The swell tracks form the starting data set used to calculate swell dissipation. Under idealized conditions and in the absence of dissipation, *Collard et al*. [2009] demonstrates that the swell energy decreases asymptotically by

$1/[\alpha\sin(\alpha)]$ for a given direction θ_0 with a spherical distance α. The term α accounts for the frequency dispersion in geographic space, and $\sin(\alpha)$ accounts for the lateral directional spreading. They also show that the difference between realistic and ideal conditions is less than 20% of the asymptotic value for distances larger than 4000 km from the storm center. Also, the effect from the nonlinear wave-wave interaction is expected to be negligible after the swells propagated beyond 4000 km [*Snodgrass et al.*, 1966].

Collard et al. [2009], *Ardhuin et al.* [2009], and *Young et al.* [2013] observed swell energy (E_s) to decay exponentially:

$$E_s(\alpha_i) = E_s(\alpha_0)\exp[-R\mu_a(\alpha_i - \alpha_0)] \tag{1}$$

with the total attenuation rate (μ_a), relative to reference spherical distance $\alpha_0 = 4000$ km, where R is the Earth radius and i represents the observation index along the transect. The effects of frequency and angular dispersion are removed by estimating the dissipation rate (μ) from

$$E_s(\alpha_i)\alpha_i\sin\alpha_i = E_s(\alpha_0)\alpha_0\sin\alpha_0\exp[-R\mu(\alpha_i - \alpha_0)]. \tag{2}$$

The rates calculated using this equation by *Ardhuin et al.* [2009] were sometimes 56 times larger than the energy loss due to shear stress theoretically derived by *Dore* [1978]

$$\mu_v = \frac{\rho_a}{\rho_w g C_g}\left(\frac{2\pi}{T}\right)^{5/2}\sqrt{2\upsilon} \tag{3}$$

where ρ_a and ρ_w are the densities of air (1026 kg m^{-3}) and water (1.3 kg m^{-3}), respectively, and υ is the air viscosity (1.4×10^{-5} m^2 s^{-1}). Note that in *Ardhuin et al.* [2009] there was a factor of 2 error in their viscous dissipation calculations [*Perignon et al.*, 2014]. Since the dissipation rates were 56 times the viscous rate, *Ardhuin et al.* [2009] suggested that swells also decay by a turbulent (nonlinear) component in the atmosphere

$$\nu = -\frac{\mathrm{d}E_s/\mathrm{d}t}{E_s} = C_g\mu = 64\frac{\rho_a\pi^2}{\rho_w g T^2} f_e u_{\mathrm{orb}} \tag{4}$$

where u_{orb} is the swell orbital velocity defined as $u_{\mathrm{orb,swell}} = 4\pi\sqrt{E_s}/T$ and f_e is the swell dissipation factor. The selection of either the viscous or turbulent decay depends on the sea surface roughness through the critical Reynolds number $Re_c = 4u_{\mathrm{orb}}a_{\mathrm{orb}}/\nu_{\mathrm{air}}$, where a_{orb} is the significant amplitude of the surface orbital displacement. This formulation improved swell prediction in the spectral wave model, WAVEWATCH III [e.g., *Ardhuin et al.*, 2010; *Stopa et al.*, 2015b]. *Babanin* [2006] suggested a similar swell decay mechanism with losses in the ocean. While it is under debate which mechanism dominates, both formulations have the same functional form and behave nonlinearly with respect to wave frequency [*Young et al.*, 2013].

In the present study, we solve the above equations by fitting a function $E_s(\alpha_i)$ for each track ensemble to estimate the total attenuation, μ_a (equation (1)); the dissipation, μ (equation (2)); and swell friction factor, f_e (equations (3) and (4)) which uses a combination of the viscous and turbulent components. We search the entire two-dimensional space from 1 to 10 m and -2×10^{-7} to 1×10^{-6} m^{-1} to find the pair ($E_s(\alpha_0)$, μ_a), ($\hat{E}_s(\alpha_0)$, μ), or ($\hat{E}_s(\alpha_0)$, f_e) that gives the minimum root-mean-square difference with the observations $E_s(\alpha_i)$. Supplementary information from the wave hindcast of *Rascle and Ardhuin* [2013] is used to calculate the Re_c to include local sea effects. Then we specifically solve

$$\mathrm{d}(E_s\alpha\sin\alpha)/\mathrm{d}\alpha = \mu_v R E_s\alpha\sin\alpha \qquad Re_c < 10^5 \tag{5}$$

or

$$\mathrm{d}(E_s\alpha\sin\alpha)/\mathrm{d}\alpha = 64\frac{\rho_a\pi^2}{\rho_w g T^2}(\kappa) f_e u_{\mathrm{orb}} \quad Re_c \geq 10^5 \tag{6}$$

where κ is a correction factor defined as the maximum of $(1.5, u_{\mathrm{orb}}/u_{\mathrm{orb,swell}})$. This factor accounts for wind seas and other swells present in the sea state that would affect the computation of f_e. We then convert the wave energy to swell wave height using $H_{ss0} = 4\sqrt{E_{s0}}$.

We take into account the uncertainty of the SAR-derived wave heights by performing Monte Carlo simulations similar to *Ardhuin et al.* [2009]. Each SAR observation (E_{si}) is perturbed using an appropriate error distribution and then minimization is performed. This process is repeated 100 times, and only the median values of H_{ss0} and μ or f_e are reported here. The supporting information gives more information.

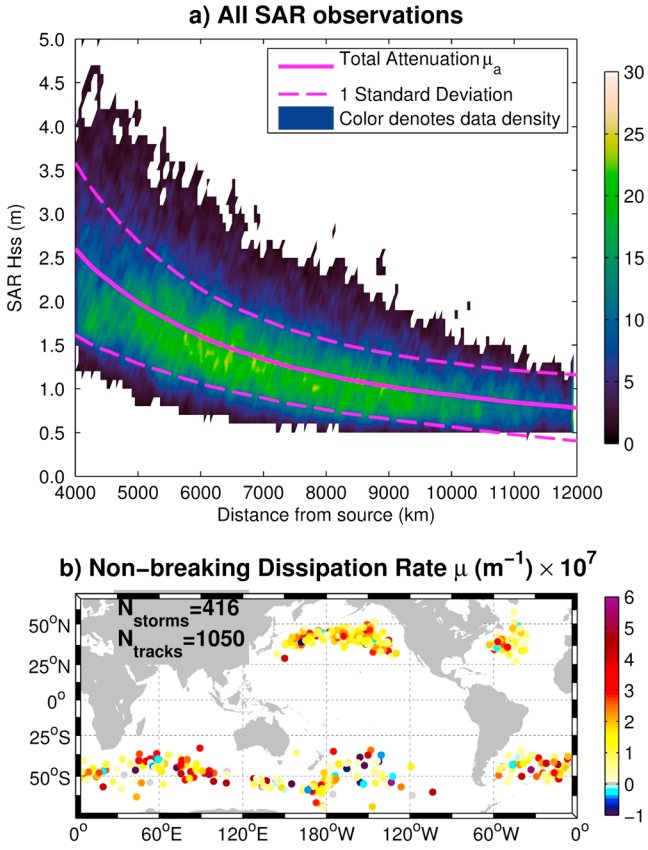

Figure 1. (a) Observed swell wave height as a function of distance from the storm source overlaid with average attenuation and one standard deviation. (b) Source locations color coded by the nonbreaking dissipation rate (equation (2)).

3. Results

Figure 1 shows all 28,062 SAR observations from 1050 tracks using 416 storms used in the analysis. Figure 1a shows the average attenuation (μ_a) given as a function of distance from the source calculated using equation (1). The exponential decay matches the swell behavior reasonably well. We limit our SAR observations to $H_{ss0} > 0.5$ m since smaller wave heights are difficult for the SAR to resolve amongst the other components. The far range (>9000 km) is impacted by this criterion, and the average decay in our depiction in Figure 1a might be overestimated in the far field. If more far-field observations were available, then the dissipation variability is expected to reduce. This is because in the far field the decay is very stable and the minimization would fit these components better.

Figure 1b displays the spatial distribution of source locations color coded by their dissipation rate (μ). There is near-homogenous distribution across the extratropics with a dense number of sources in the North Pacific, Eastern North Atlantic, and dispersed across the Southern Ocean. There is a lack of sources in the western half of the South Pacific and North Atlantic because storms often follow the same trajectories creating overlapping swells and makes the identification of a unique source difficult. Furthermore, storms located in western portion of the basins send swells across the oceans with lifetimes exceeding 1 week. Thus, the SAR has a higher probability to sample these events compared to sources in the eastern portion. The sources presented here give a robust sample of the ocean in relation to the previous studies of *Snodgrass et al.* [1966] and *Ardhuin et al.* [2009] which were based on a small sample size and mostly in the Pacific.

The large number of events provides the first statistically representative estimation of swell dissipation rates. Figure 2 displays the probability density distributions of the dissipation rates (μ, μ_a), swell friction factor f_e, and ratio of μ/μ_v. A two-parameter gamma distribution was fitted to these distributions. In total, there are 910 events with positive dissipation and 140 events with negative values, while 423 are not statistically different from zero. This leaves 606 positive and 21 negative events, with significant dissipation rates at the 95% confidence limit. The negative events still have decreasing wave heights due to frequency dispersion and angular spreading. The total attenuation rate, μ_a, has median of 3.2×10^{-7} m^{-1}, while the dissipation rate is 1.0×10^{-7} m^{-1}. Therefore, to a leading order, the reduction of the swell height is related to the frequency dispersion and spreading effects. When $\alpha < \pi/2$, the angular spreading attenuation dominates in the near field since the decay behaves like $1/\sin\alpha$.

Figure 2 (middle) presents the nonlinear dissipation friction factor f_e which is often a key parameter in practical wave modeling. Our data span $-0.01 \le f_e \le 0.024$ with a median of 0.0037, and the majority of the data (~79%) are within 0.001 to 0.007 which lie within the smooth range of *Jensen et al.* [1989] (0.002 to 0.008). Our friction factors have a larger range than those of *Ardhuin et al.* [2009] $-0.001 \le f_e \le 0.019$, and our median of 0.0037 is almost half of theirs. This discrepancy arises because the 22 events of *Ardhuin et al.* [2009] were stronger events. The top axis presents the corresponding friction factor, b_1 ($b_1 = 24 f_e \rho_a / \rho_w$), proposed by

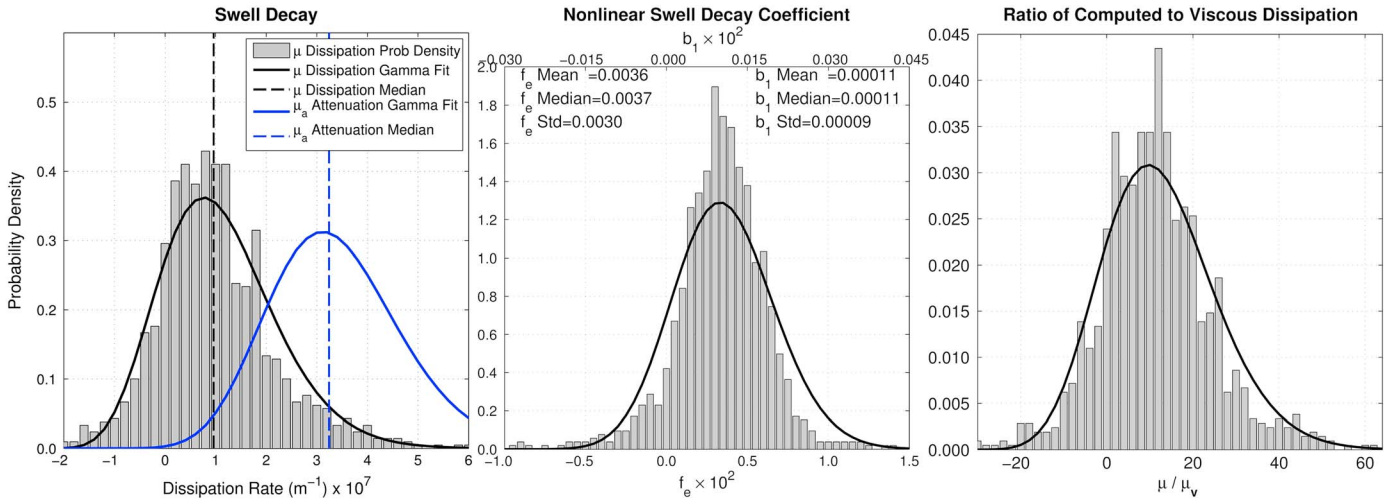

Figure 2. Probability density functions of the (left) attenuation and nonbreaking dissipation (μ_a, μ), (middle) swell friction factor (f_e), and (right) ratio of nonbreaking to viscous dissipation (μ/μ_v).

Babanin [2006]. The b_1 median equals 1.1×10^{-4} an order of magnitude lower than *Young et al.* [2013]. However, these authors did not remove the dominant effects of frequency dispersion and angular spreading.

Lastly, Figure 2 (right) gives the statistical distribution of the ratio of computed to the viscous dissipation. This ratio shows that the swell decay is often 2 to 22 times larger than (linear) viscous decay, suggesting that the swell decay mechanism is more effective at removing energy than through viscous losses. This led *Ardhuin et al.* [2009] to suggest a laminar to turbulent swell decay mechanism because it can explain the large range, and the turbulent component is nonlinear and thus more effective at dissipating the energy. The majority of our rates are 0 to 20 times the viscous rate with a median of 12. There are few instances of extreme dissipation exceeding 60 times the viscous rate, but none exceed 66 suggesting an upper limit.

The swell dissipation rates computed here represent an average decay rate for each trajectory based on at least 15 (and few exceed 40) observations. The SAR data are discrete locations, and full time history of the swell evolution is missed. Therefore, we explore the relationship between the dissipation rates and the environmental conditions along the swell trajectories by interpolating wind and wave information from the hindcast of *Rascle and Ardhuin* [2013]. The hope is to provide some insights on the swell decay mechanism as a function of the environmental conditions where the swell propagates.

The variables given in Table 1 are interpolated along each track every 50 km from $\alpha = 4000$ km to the last SAR observation. Next we integrate the variables along the trajectories. In addition, the Reynolds number, swell wave height, and swell steepness at 4000 km are included. Table 1 gives the correlation coefficients between the dissipation rate and the variables. Most of the correlation coefficients are weak (<0.5), and the wave

Table 1. Correlation Coefficients for a Range of Variables Integrated Along Each Swell Track Versus the Nonbreaking Dissipation Rate

Variable Integrated Along Track	Weighted With Magnitude	Angle	Weighted With Magnitude and Direction
Significant wave height (H_s)	−0.138*	$\cos(\theta_{swell}\text{-}\theta_{average})$	−0.146*
Wind-sea significant wave height (H_{sww})	−0.075	$\cos(\theta_{swell}\text{-}\theta_{wind\ wave})$	0.098
Orbital wave velocity (U_{orb})	−0.117*	$\cos(\theta_{swell}\text{-}\theta_{U10})$	−0.254*
Stokes drift (U_{ss})	−0.107*	$\cos(\theta_{swell}\text{-}\theta_{Uss})$	−0.167*
Mean square slope (M_{ss})	−0.089	$\cos(\theta_{swell}\text{-}\theta_{Mss})$	+0.117*
Wind speed (U_{10})	−0.092	$\cos(\theta_{swell}\text{-}\theta_{U10})$	−0.295*
Wave age (WA)	−0.098	$\cos(\theta_{swell}\text{-}\theta_{average})$	−0.065
Swell Reynolds number at 4000 km (Re)	−0.140*	-	-
Swell wave height at 4000 km (H_o)	+0.380*	-	-
Wave steepness at 4000 km (S)	+0.424*	-	-

*Statistical significance at the 99.9% limit.

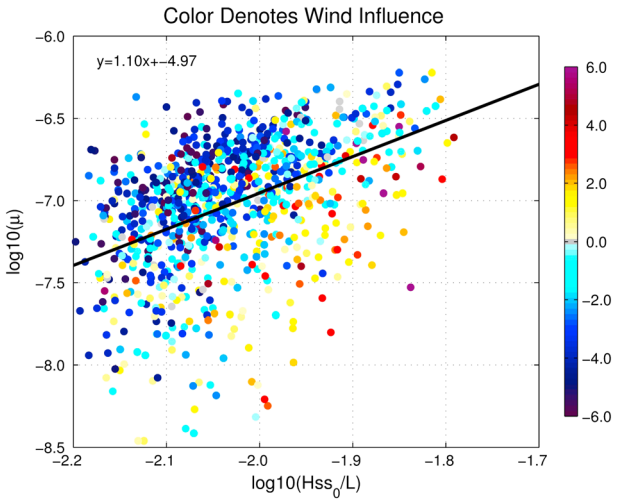

Figure 3. Estimated swell dissipation for the 910 positive events plotted as function of the initial swell slope (H_{ss0}/L) taken at 4000 km from the storm center on a logarithmic plot. The wind influence is the integration of $U_{10}\cos(\varphi)$ along the swell trajectory where φ is the angle between the wind and swell direction.

steepness is the largest. However, the majority of this correlation comes from the inherent relationship with the swell height, H_{ss0}, since the wavelengths have a small range 13–18 s. When the variables are weighted with their relative angle from the swell, $\cos(\theta_{swell}\text{-}\theta_{variable})$, the strength of the relationship increases. This suggests the relative direction between the swell and local wind or wave conditions plays a role in the dissipation. Besides the wave steepness, swell height, the orbital wave velocity and wind speed weighted with the wind direction give the strongest relationships.

Figure 3 explores the relationship between the swell dissipation, wave steepness, and wind interaction, restricted to positive rates. Steeper waves generally correspond to enhanced dissipation rates, but the steepness only explains a fraction of the variance. A crude linear relationship exists for swell dissipation rates from $10^{-7.5}$ to $10^{-6.5}\,m^{-1}$ and is plotted for reference. From this depiction it is clear that there is a lot of variability in μ, owing to the complexity of the problem and large range of decay rates. In addition, when the wavelengths are larger, the variability reduces because the point source assumption is better suited for the stronger events that also produce longer wavelengths. The majority of the events have opposing winds (70%). *Snodgrass et al*. [1966] proposed that waves with opposite winds decay more effectively than following winds. However, their data set was not able support this claim. Our use of 910 events enables us to see that there is a weak relationship between opposing wind events (negative values) and higher dissipation rates. On the other hand, cases when the wind follows the waves (positive values) there is weaker dissipation despite the large spread. The wave orbital velocity weighted with the wind direction shows a similar relationship (not shown).

4. Discussion and Conclusion

Ocean swells were systematically tracked using spectra from Envisat ASAR wave mode from 2003 to 2012 consisting of 1050 events from 460 unique storm events. We take advantage of the satellite observations to track individual swell packets extending the previous works of *Snodgrass et al*. [1966] and *Ardhuin et al*. [2009], which had been limited in quantity. This allowed us to observe the statistical distribution of the swell decay from a robust sample including all major wave generation regions in the Pacific, Atlantic, and Indian Oceans.

The majority of the dissipation rates lie within the range from 0 to $2\times10^{-7}\,m^{-1}$ with a large scatter. The frequency dispersion and angular spreading causes must be removed before swell dissipation is calculated consistent with *Collard et al*. [2009]. The SAR observations are imprecise (the RMS error is 25% of the measured value), and this contributes to the noise of swell dissipation estimates. In addition, we expect that if more far-field observations (>9000 km) were available, then the variability would reduce since the far-field observations are relatively stable. We assume all waves are generated at the same time and propagate along great circles. While evidence shows that this assumption is valid in deep water, large distances from islands, and in the absence of currents [e.g., *Snodgrass et al*., 1966; *Collard et al*., 2009; *Gallet and Young*, 2014], it introduces errors into our estimates, and we have not quantified the errors due to currents.

We estimate some negative dissipation rates which would equate to swell growth, which cannot be ruled out (e.g., the effect of wind stress modulation in *Hasselmann* [1971] or the work of the Stokes drift shear against the wind stress in *Ardhuin and Jenkins* [2006]). Yet our assumption of dispersion effects producing a decay like $1/[\alpha\sin(\alpha)]$ is valid under idealized conditions when swells propagate on a sphere without obstructions. Once

a swell is confined, say, due to the presence of an island, then this assumption might no longer be valid. Possibly, some of the negative (and positive) swell dissipation cases are incorrect due to this effect. The population of statistically significant negative events is small and consists of 21 cases (2% of the population). Our analysis of these events did not provide any insights to the physical processes, and further studies are warranted to describe their behavior.

We observe that the dissipation is often 12 times the viscous rate supporting a stronger dissipation mechanism such as *Ardhuin et al*. [2009] or *Babanin* [2006] wave-induced turbulence in the ocean boundary layer. The viscous rate is approximately $10^{-8}\,\mathrm{m}^{-1}$ or smaller, while the swell dissipation rates here are $10^{-7}\,\mathrm{m}^{-1}$. The SAR H_{ss} precision limits our dissipation precision to $\sim 10^{-7}\,\mathrm{m}^{-1}$ (see supporting information); therefore, it is impossible to distinguish between the viscous or turbulent cases or make any further conclusions of the exact transition (i.e., Re_c) between the two regimes. If the SAR precision improves, then we might be able to determine the more appropriate swell decay mechanism: the turbulent boundary layer in the ocean or atmosphere. This is because the *Babanin* [2006] Re_c is 10^3, while the *Ardhuin et al*. [2009] Re_c is 10^5. Current and future missions of Sentinel-1A and CFOSAT might allow more precise estimates, which would further benefit from field campaigns designed to observe swell along great circle routes, with simultaneous measurements of air-sea interface processes.

We sought to establish a relationship between swell decay and other wind and wave parameters by integrating the environmental conditions from wave model simulations along the swell trajectories. Out of all variables tested, the wave steepness, swell height, wind speed, and orbital wave velocity weighted with the relative wind direction have the strongest correlation to the swell dissipation rate. It is seen that the relative direction between the wind and waves influences the rate of swell decay. Since none of the variables tested had a strong relationship, it can be argued that more precise SAR observations are required or our averaged-track approach is not accurate enough at the scales of important physical processes. A full description of the air-sea energy and momentum exchange is needed similar to the numerical modeling efforts of *Perignon et al*. [2014] or the theoretical derivation of *Kudryavtsev and Makin* [2004].

The swell dissipation rate investigated here is an important parameter in several applications, since it represents energy released to the air-sea interface. Regardless of the mechanism or physical processes involved, the dissipation rate is particularly important for theoretical studies and numerical models [*Kudryavtsev and Makin*, 2004; *Hanley and Belcher*, 2008; *Ardhuin et al*., 2010]. The swell dissipation rates for waves with $13 < T < 18\,\mathrm{s}$ and associated parameters, derived from our study, are $\mu \approx 1 \times 10^{-7}\,\mathrm{m}^{-1}$, $f_e \approx 0.004$, and $b_1 \approx 0.0001$. These rates and associated ranges presented here can be used for practical applications, such as wave modeling and coupling ocean-wave-atmosphere models. Although there is a large variability in these estimates, as seen in Figure 3, and many statistically significant rates on the order of $10^{-8}\,\mathrm{m}^{-1}$, the present observations and analysis give a more robust estimate of the swell dissipation range than previous studies. Future investigations with more accurate observations would be essential to improve our understanding of air-sea fluxes and obtain a more complete description of processes governing swell decay, as well as more accurate dissipation rates for practical applications.

Acknowledgments
JS is supported by LabexMER via grant ANR-10-LABX-19-01, and EU-FP7 project SWARP under grant agreement 607476. We would like to thank the two anonymous reviewers for their comments that have improved this paper. The Envisat SAR data sets are made available through the European Space Agency through the GlobWAVE project (http://globwave.ifremer.fr/), and the wave model data are available by the Integrated Ocean Waves for Geophysical and other Applications (IOWAGA) project: ftp.ifremer.fr/ifremer/cersat/products/gridded/wave-watch3/HINDCAST/.

References

Alves, J.-H. G. M. (2006), Numerical modeling of ocean swell contributions to the global wind-wave climate, *Ocean Modell.*, *11*(1–2), 98–112, doi:10.1016/j.ocemod.2004.11.007.

Ardhuin, F., and A. D. Jenkins (2006), On the interaction of surface waves and upper ocean turbulence, *J. Phys. Oceanogr.*, *36*, 551–557.

Ardhuin, F., B. Chapron, and F. Collard (2009), Observation of swell dissipation across oceans, *Geophys. Res. Lett.*, *36*, L06607, doi:10.1029/2008GL037030.

Ardhuin, F., et al. (2010), Semi-empirical dissipation source functions for ocean waves. Part I: Definition, calibration, and validation, *J. Phys. Oceanogr.*, *40*(9), 1917–1941.

Ardhuin, F., F. Collard, B. Chapron, F. Girard-Ardhuin, G. Guitton, A. Mouche, and J. E. Stopa (2015), Estimates of ocean wave heights and attenuation in sea ice using the SAR wave mode on Sentinel-1A, *Geophys. Res. Lett.*, *42*, 2317–2325, doi:10.1002/2014GL062940.

Babanin, A. V. (2006), On a wave-induced turbulence and a wave-mixed upper ocean layer, *Geophys. Res. Lett.*, *33*, L20605, doi:10.1029/2006GL027308.

Babanin, A. V., and B. K. Haus (2009), On the existence of water turbulence induced by non-breaking surface waves, *J. Phys. Oceanogr.*, *39*, 2675–2679.

Barber, N. F., and F. Ursell (1948), The generation and propagation of ocean waves and swell I wave periods and velocities, *Philos. Trans. R. Soc. London, 240A*, 527–560.

Chapron, B., H. Johnsen, and R. Garello (2001), Wave and wind retrieval from SAR images of the ocean, *Ann. Telecommun.*, *56*, 682–699.

Chen, G., B. Chapron, R. Ezraty, and D. Vandemark (2002), A global view of swell and wind sea climate in the ocean by satellite altimeter and scatterometer, *J. Atmos. Oceanic Technol.*, *19*(11), 1849–1859.
Collard, F., F. Ardhuin, and B. Chapron (2009), Monitoring and analysis of ocean swell fields from space: New methods for routine observations, *J. Geophys. Res.*, *114*, C07023, doi:10.1029/2008JC005215.
Dore, B. D. (1978), Some effects of the air-water interface on gravity waves, *Geophys. Astrophys. Fluid Dyn.*, *10*, 215–230.
Fairall, C. W., E. F. Bradley, J. E. Hare, A. A. Grachev, and J. B. Edson (2003), Bulk parameterization of air–sea fluxes: Updates and verification for the COARE algorithm, *J. Clim.*, *16*(4), 571–591, doi:10.1175/1520-0442(2003)016<0571:BPOASF>2.0.CO;2.
Gallet, B., and W. R. Young (2014), Refraction of swell by surface currents, *J. Mar. Res.*, *72*, 105–126.
Hanley, K. E., and S. E. Belcher (2008), Wave-driven wind jets in the marine atmospheric boundary layer, *J. Atmos. Sci.*, *65*, 2646–2660.
Harris, D. L. (1966), The wave-driven wind, *J. Atmos. Sci.*, *23*, 688–693.
Hasselmann, K. (1971), On the mass momentum transfer between short gravity waves and larger-scale motions, *J. Fluid Mech.*, *50*(1), 189–205.
Hasselmann, K., et al. (2012), The ERS SAR wave mode—A breakthrough in global ocean wave observations, in *ERS Missions—20 Years of Observing Earth*, *ESA Sci. Public. SP-1326*, pp. 1–38, ESA, Noordwijk, Netherlands.
Heimbach, P., and K. Hasselmann (2000), Development and application of satellite retrievals of ocean wave spectra, in *Satellites, Oceanography and Society*, edited by D. Halpern, pp. 5–33, Elsevier, Amsterdam.
Hoeke, R. K., K. L. McInnes, J. C. Kruger, R. J. McNaught, J. R. Hunter, and S. G. Smithers (2013), Widespread inundation of Pacific Islands triggered by distant-source wind-waves, *Global Planet. Change*, *108*, 128–138.
Högström, U., A. S. Smedman, E. Sahlee, W. M. Drennan, K. K. Kahma, C. Johansson, H. Pettersson, and F. Zhang (2009), The atmospheric boundary layer during swell—A field study of the governing mechanism, *J. Atmos. Sci.*, *66*, 2764–2779.
Holt, B., A. K. Liu, D. W. Wang, A. Gnanadesikan, and H. S. Chen (1998), Tracking storm-generated waves in the northeast Pacific Ocean with ERS-1 synthetic aperture radar imagery and buoys, *J. Geophys. Res.*, *103*, 7917–7929.
Husson, R. (2012), Development and validation of a global observation-based swell model using wave mode operating Synthetic Aperture Radar, PhD thesis, Dep. of Earth Sci., Univ. of Bretagne Occidentale, Brest, France.
Jensen, B. L., B. M. Sumer, and J. Fredsoe (1989), Turbulent oscillatory boundary layers at high Reynolds numbers, *J. Fluid Mech.*, *206*, 265–297.
Kerbaol, V., B. Chapron, and P. Vachon (1998), Analysis of ERS-1/2 synthetic aperture radar wave mode imagettes, *J. Geophys. Res.*, *103*, 7833–7846.
Kudryavtsev, V. N., and V. K. Makin (2004), Impact of swell on the marine atmospheric boundary layer, *J. Phys. Oceanogr.*, *34*, 934–949.
Lefevre, J.-M. (2009), High swell warnings in the Caribbean Islands during March 2008, *Nat. Hazards*, *49*(2), 361–370.
Lehner, S., J. Schulz-Stellenfleth, B. Schattler, and J. Horstmann (2000), Wind and wave measurements using complex ERS-2 SAR wave mode data, *IEEE Trans. Geosci. Remote Sens.*, *38*(5), 2246–2257.
Munk, W. M. (1947), Tracking storms by forerunners of swell, *J. Meteorol.*, *4*(2), 45–57.
Munk, W. M., G. R. Miller, F. E. Snodgrass, and N. F. Barber (1963), Directional recording of swell from distant storms, *Philos. Trans. R. Soc. London*, *A255*, 505–584.
Perignon, Y., F. Ardhuin, M. Cathelain, and M. Robert (2014), Swell dissipation by induced atmospheric shear stress, *J. Geophys. Res. Oceans*, *119*, 6622–6630, doi:10.1002/2014JC009896.
Portilla, J., F. J. Ocampo-Torres, and J. Monbaliu (2009), Spectral partitioning and identification of wind sea and swell, *J. Atmos. Oceanic Technol.*, *26*, 107–122.
Rascle, N., and F. Ardhuin (2013), A global wave parameter database for geophysical applications. Part 2: Model validation with improved source term parameterization, *Ocean Modell.*, *70*, 174–188.
Semedo, A., Ø. Sætra, A. Rutgersson, K. Kahma, and H. Pettersson (2009), Wave induced wind in the marine boundary layer, *J. Atmos. Sci.*, *66*, 2256–2271.
Snodgrass, F. E., G. W. Groves, K. Hasselmann, G. R. Miller, W. H. Munk, and W. H. Powers (1966), Propagation of ocean swell across the Pacific, *Philos. Trans. R. Soc. London, Ser. A*, *249*, 431–497.
Stopa, J. E., F. Ardhuin, B. Chapron, and F. Collard (2015a), Estimating wave orbital velocity through the azimuth cutoff from space borne satellites, *J. Geophys. Res. Oceans*, *120*, 7616–7634, doi:10.1002/2015JC011275.
Stopa, J. E., F. Ardhuin, A. V. Bababin, and S. Zieger (2015b), Comparison and validation of physical parameterizations in spectral wave models, *Ocean Modell.*, doi:10.1016/j.ocemod.2015.09.003.
Young, I. R., and R. J. Sobey (1985), Measurements of the wind-wave energy flux in an opposing wind, *J. Fluid Mech.*, *151*, 427–442.
Young, I. R., A. V. Babanin, and S. Zieger (2013), The decay rate of ocean swell observed by altimeter, *J. Phys. Oceanogr.*, *43*, 2322–2333.